Multi-channel DFB laser array fabricated by SAG with optimized epitaxy conditions

Can Zhang (张 灿), Song Liang (梁 松)*, Li Ma (马 丽), Liangshun Han (韩良顺), and Hongliang Zhu (朱洪亮)

Key Laboratory of Semiconductors Materials, Institute of Semiconductors, Chinese Academy of Sciences, Beijing 100083, China

**Corresponding author: liangsong@semi.ac.cn*

Received September 27, 2012; accepted November 16, 2012; posted online March 6, 2013

Selective area growth (SAG) is performed to fabricate monolithically integrated distributed feedback (DFB) laser array by adjusting the width of a SiO_2 mask. A strain-compensated-barrier structure is adopted to reduce the accumulated strain and improve the quality of multi-quantum well materials. Varying the strip width of the SAG masks, the DFB laser array with an average channel spacing of 1.47 nm is demonstrated by a conventional holographic method with constant-pitch grating. The threshold current from 14 to 18 mA and over 35-dB side mode suppression ratio (SMSR) are obtained for all DFB lasers in the array.

OCIS codes: 140.2010, 140.3570, 250.5300, 250.5960.
doi: 10.3788/COL201311.041401.

Monolithically integrated distributed feedback (DFB) laser array has an important role in the modern wavelength division multiplexing (WDM) system, which makes optical networks cost-effective, reliable, and lowers the power consumption to greatly enhance their performance[1−5].

Several techniques have been proposed for the fabrication of DFB laser array, such as electron beam lithography[6−8], ridge width variation[9], reconstruction equivalent chirp (REC) technology[10], sampled gratings[11], post-growth fabrication[12], and thermal tuning[13,14]. However, most of these techniques require high costs and harsh manufacture. The high cost and low yield of the laser arrays hinder their wide application. Thus, a simple fabrication technology is urgently needed for the production of a high-yield and low-cost DFB laser array.

Selective area growth (SAG) using metal organic vapor phase epitaxy (MOVPE) is an attractive method to fabricate monolithically integrated devices[15−17]. In this technique, epitaxial layers are grown in the areas between dielectric masks. The thickness enhancement factors of the selectively grown layers are affected by the geometry of mask patterns, including mask widths and the mask gap between two adjacent mask patterns. For multi-quantum well (MQW) materials, the varied thickness and composition cause an emission wavelength shift. The effective refractive index of MQWs may be controlled by modulating the thickness of the waveguide layer, which may control the lasing wavelength.

In this letter, a tensile strained barrier layer is added to obtain a wide working range for optimizing SAG epitaxy conditions. Multi-wavelength DFB laser array, with an average channel spacing of 1.47 nm, is demonstrated using a conventional holographic method with constant-pitch grating. In the array, the threshold currents of the DFB lasers are between 14 and 18 mA, and the side mode suppression ratio (SMSR) of all the laser spectra is above 35 dB.

The dielectric masks used for the SAG study are SiO_2 grown via plasma-enhanced chemical vapor deposition (PECVD). The thickness of the film is 150 nm. The parallel pairs of the mask strips with 250-μm period are patterned by photolithography and HF wet etching in the [110] direction. An AXITRON close coupled showerhead (CCS) MOVPE reactor as used for the SAG study, with the growth temperature kept at 640 °C. The MQWs comprise six compressively strained InGaAsP wells (+1.1 $\times 10^{-2}$, $\lambda_{PL} = 1.59$ μm) and seven InGaAsP barrier layers, and are sandwiched between two 80-nm InGaAsP separate confinement heterostructure (SCH) layers ($\lambda_{PL} = 1.2$ μm) lattice matched to the InP. In unpatterned substrates, the thickness of the well and barrier are 5 and 10 nm, respectively. The emission wavelength and intensity of the SAG MQWs were studied by micro-area photoluminescence (PL).

The PL emission wavelength in the SAG region exhibits a red shift correlating to the mask patterns. The red shift is mainly caused by the SAG, which induces the thickness enhancement and indium enrichment of the quantum wells (QWs) in the selective grown region[18]. Figure 1 schematically shows the mask pattern for SAG. For the material growth study, the width of the mask gap (W_0) is kept constant at 20 μm, and the width of mask strips (W_m) ranges from 1 to 34 μm in 1 μm increment. The period of the adjacent mask is 250 μm.

Comprehensively strained QWs were grown to improve the quantum efficiency and reduce the threshold current density of the laser device. Figure 2 shows the PL wavelength variation with the width of mask strip (W_m) when

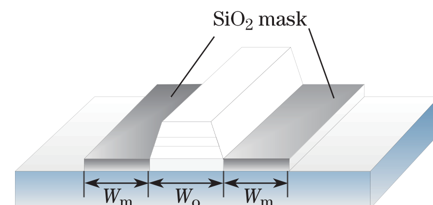

Fig. 1. Mask pattern for selective area growth.

 © 2013 Chinese Optics Letters

the barriers of the QWs are 1.2 Q layer matched to the InP. The total red shift of the PL wavelength is about 100 nm (from 1 483 to 1 583 nm), which shows a slope of 4.62 nm/μm. However, the PL intensity of the SAG MQWs exhibits a steep decline as the strip width increased, dropping by 60% when the strip-width exceeds 15 μm. This occurrence is caused by the increase of the accumulated strain in SAG MQWs as the thickness of the MQWs increases with the strip width, leading to the rapid degradation of the material quality. Tensile-strained barriers (about 0.3% tensile strain) were used to compensate the compressive strain of the QWs to reduce the effect of accumulated strain. Figure 3 shows the results of PL spectra of the strain-compensated MQWs. The degradation of PL intensities with the increase in stripe width is less than 40% until the strip-widths (W_{m}) reached up to 27 μm. The quality of the MQW materials showed an obvious improvement with the strain compensation.

The effective index method (EIM) is a well-known approximate analytical approach for the theoretical study of optical waveguides, which is used to analyze the structure of ridge-waveguide laser[19,20].

Figure 4 shows the ridge waveguide structure and its equivalent slab waveguide. A composite slab with vertical walls whose width is equal to that of the ridge waveguide was formed using the effective refractive indices calculated. The material thickness of each layer has been given in the aforementioned paragraphs. For the calculation, the refractive index was set as follows: $n_1 = n_{32} = 3.167$ for the InP, $n_{21} = n_{23} = 3.339$ for the SCH, $n_{31} = n_{33} = 1$ for air, and $W = 3$ μm. The effective refractive index of the MQW region was obtained by

$$n_{22} = \sqrt{(H_{\mathrm{w}} \cdot n_{\mathrm{w}}^2 + H_{\mathrm{b}} + H_{\mathrm{w}} \cdot n_{\mathrm{b}}^2)/(H_{\mathrm{w}} + H_{\mathrm{b}})}, \quad (1)$$

where n_{w} and n_{b} are the refractive indices of the well and the barrier, respectively, and t_{w} and t_{b} are the thicknesses of the well and the barrier, respectively. In Eq. (1), n_{w} and n_{b} are 3.587 and 3.339, respectively. Using the thickness enhancement factor, the refractive index of the ridge waveguide for each selective grown region was calculated by EIM. The results are given in Fig. 5, which shows an

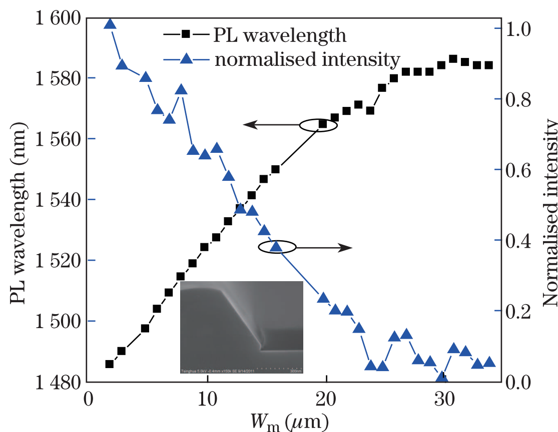

Fig. 2. PL wavelength and normalized intensity versus strip width W_{m} without strain compensation. The subgraph is the side morphology for the SAG material.

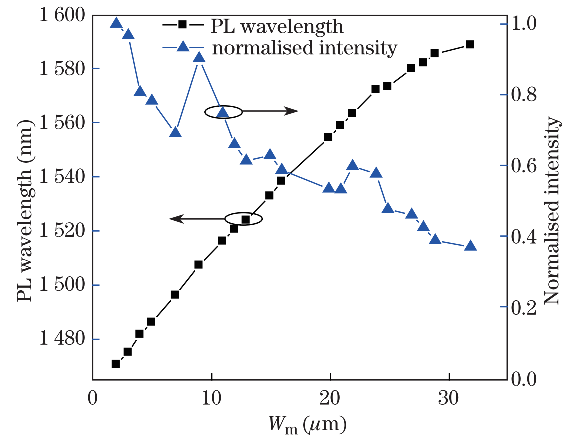

Fig. 3. PL wavelength and normalized intensity versus strip width W_{m} with strain compensation.

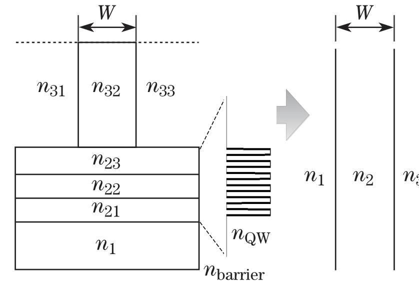

Fig. 4. Ridge waveguide structure and its equivalent slab waveguide by EIM.

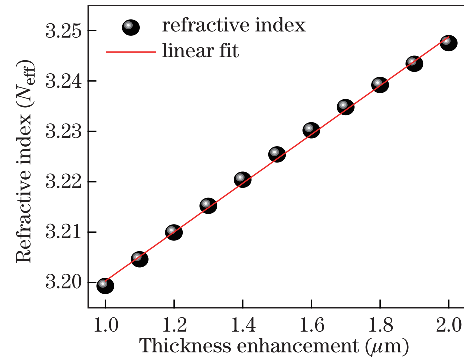

Fig. 5. Calculated refractive index versus the thickness enhancement factor by EIM.

approximately linear relationship between the refractive index and thickness enhancement factor, with a linear fitting slope of 0.053.

The thickness enhancement factors of the selectively grown layers were determined by the geometry of the mask patterns, including the mask width gap (W_0). The thickness enhancement factor of the InGaAsP material was measured when the SAG masks with $W_0 = 30$ μm and 250-μm pair separation was used. The experimental results of the thickness enhancement factor are given in Fig. 6, which show a good linearity with a linear fitting slope of about 0.02 μm. Thus, the effects of varying the strip width of SAG on the effective refractive index may be estimated, as shown in Figs. 5 and 6. The lasing wavelength of the DFB laser was determined by

$$\lambda i = 2N_{\mathrm{eff}i} \cdot \Lambda, \quad (2)$$

where λ_i and $N_{\mathrm{eff}i}$ are the lasing wavelength and the effective refractive index of the ith channel and Λ is the period of the grating. Therefore, the wavelength λ_i of the ith channel was calculated by the strip width W_{m}, as shown in Figs. 5 and 6.

The materials of the multi-channel DFB array were grown via a two-step MOVPE. In the first step, a low SCH layer, a MQW layer, an upper SCH layer, and a p/n doped InGaAsP layer were grown successively on an n-InP substrate with the dielectric mask patterns. A grating with a uniform pitch was then formed on the entire wafer using a holographic lithograph. The reverse junction in the InGaAsP layer induces a partial gain coupling into the DFB structure, which increases the single mode lasing rate of the device. Afterward, a second epitaxy growth follows, including a p-type InP cladding layer and a p^+ InGaAs contact layer. A wet etching process was applied to fabricate the ridge waveguide structure. A 350-nm-thick SiO_2 was used as passivation layer for the ridges. After the SiO_2 on the top of ridges was removed, the Ti-Au p-contacts were formed through thermal evaporation. AuGeNi alloy as deposited as n-contact metal after the wafer was thinned to about 150 μm. For characterization, the laser arrays were cleaved to obtain a 300-μm cavity length. Both facets were left uncoated.

SAG masks with 30-μm opening were used for the fabrication of the laser array. Compared with the MQW materials with 20-μm opening, the PL intensity decrease of the MQWs with 30-μm opening was relatively slower as W_{m} increased. This result may be attributed to the following reason. The growth rate of the QWs between the SAG patterns is larger than that of the QWs at a non-SAG area, and the trend is more prominent in a smaller W_0. At a higher growth rate, the effective diffusion length of the adatoms is reduced, leading to the introduction of dislocations in the materials[21], thereby resulting in the degradation of the material quality. With the fixed growth rate of the QWs at a non-SAG area, a smaller W_0 leads to a faster increase of the growth rate with W_{m} and also a faster quality degradation of the SAG QWs with W_{m}. The increase in the strip width is designed to be 2.8 μm and the W_{m} is 12.2 μm for the channel 1. According to Figs. 5 and 6 and Eq. (2), the expected wavelength spacing between adjacent channels is about 1.43 nm by numerical calculation.

The light output power versus injection current (P-I)

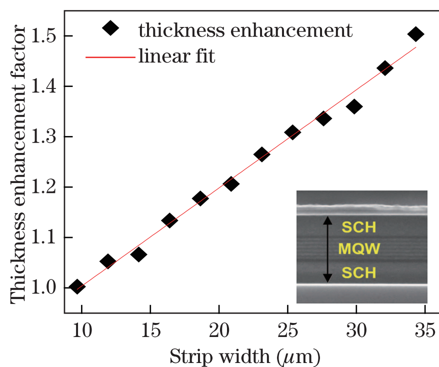

Fig. 6. Experimented thickness enhancement factor versus the strip width at $W_0 = 30$ μm. The subgraph is the SEM image of MQW for SAG.

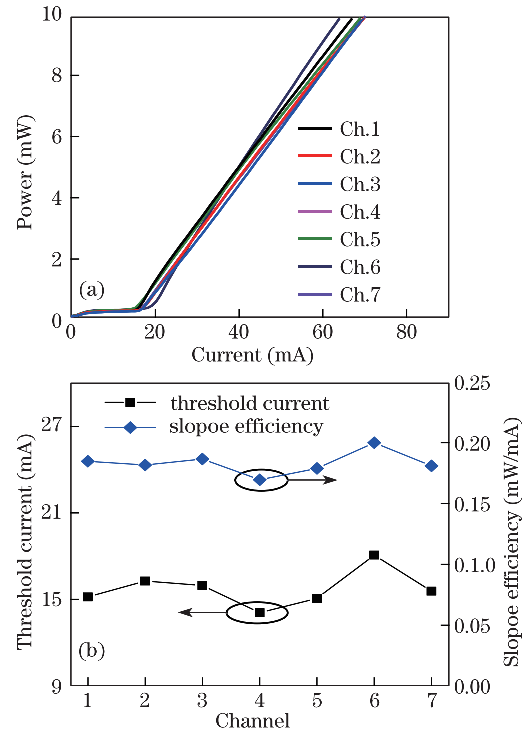

Fig. 7. (Color online) (a) P-I curves of the device at room temperature; (b) distribution of threshold current and slope efficiency for a seven-channel DFB array.

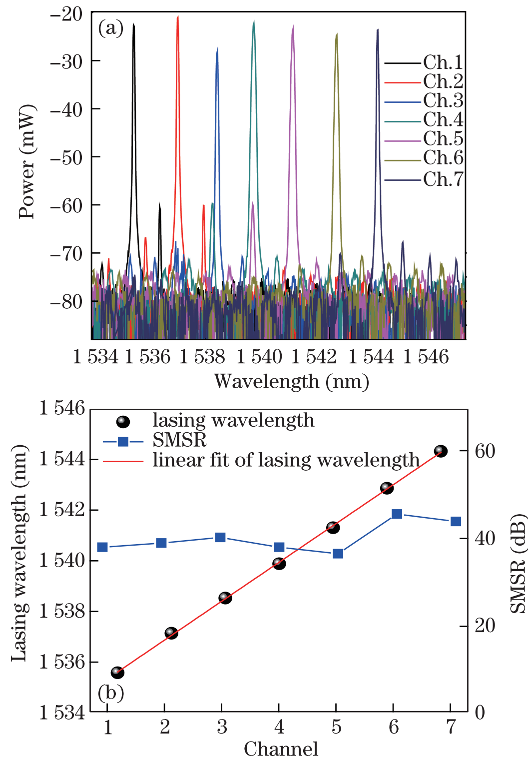

Fig. 8. (Color online) (a) Superposition of spectrum of a seven-channel DFB array; (b) distribution of lasing spectrum and SMSR for the device.

curves of a typical seven-channel laser array are shown in Fig. 7(a), where the P-I properties, measured at room temperatures with no temperature control, showed good uniformity. The distribution of threshold currents and

slope efficiencies for the seven-channel DFB laser array is shown in Fig. 7(b). The threshold currents were from 14 to 18 mA and the slope efficiency fluctuates at around 0.18 W/A.

By injecting about 60-mA current into each channel, the light of each laser of the array is coupled into a single mode fiber and characterized by an optical spectrum analyzer. Figure 8(a) shows the superimposed output spectra of the seven-channel DFB laser array. Figure 8(b) shows that the SMSR of all the channels is larger than 35 dB. The emission wavelength, as a function of channel number, is also shown in Fig. 8(b) and is best fitted with a linear fitting curve. An average channel spacing of 1.47 nm was determined close to the designed value (1.43 nm) as the strip width increased to 2.8 μm. The data shown in Fig. 8 indicated that laser arrays with uniform channel spacing can be fabricated by varying the strip width of the SAG masks. The techniques for fine tuning of laser wavelength such as heating may be used to align the emission of the array to a specific grid.

In conclusion, the SAG of the MQW materials by MOCVD are studied. The strain-compensated structure greatly improves the quality of the MQW materials when the width of the SAG mask is large. The DFB laser array with an average channel spacing of 1.47 nm is fabricated by the SAG technique, with only a constant-pitch grating fabricated by a conventional holographic method. Therefore, the SAG technique is convenient and cost-effective for the fabrication of multi-wavelength light source used in modern WDM system.

This work was supported by the National “863” Project of China (Nos. 2011AA010303 and 2012AA012203), the National Natural Science Foundation of China (Nos. 61021003 and 61090392), and the National “973” Program of China (No. 2011CB301702).

References

1. Y. Suzaki, H. Yasaka, H. Mawatari, K. Yoshino, Y. Kawaguchi, S. Oku, R. Iga, and H. Okamoto, IEEE J. Sel. Top. Quantum Electron. **11,** 43 (2005).
2. R. Nagarajan, C. H. Joyner, R. P. Schneider, J. S. Bostak, T. Butrie, A. G. Dentai, V. G. Dominic, P. W. Evans, M. Kato, M. Kauffman, D. J. H. Lambert, S. K. Mathis, A. Mathur, R. H. Miles, M. L. Mitchell, M. J. Missey, S. Murthy, A. C. Nilsson, F. H. Peters, S. C. Pennypacker, J. L. Pleumeekers, R. A. Salvatore, R. K. Schlenker, R. B. Taylor, T. Huan-Shang, M. F. Van Leeuwen, J. Webjorn, M. Ziari, D. Perkins, J. Singh, S. G. Grubb, M. S. Reffle, D. G. Mehuys, F. A. Kish, and D. F. Welch, IEEE J. Sel. Top. Quantum Electron. **11,** 50 (2005).
3. D. F. Welch , F. A. Kish, S. Melle, R. Nagarajan, M. Kato, C. H. Joyner, J. L. Pleumeekers, R. P. Schneider, J. Back, A. G. Dentai, V. G. Dominic, P. W. Evans, M. Kauffman, D. J. H. Lambert, S. K. Hurtt, A. Mathur, M. L. Mitchell, M. Missey, S. Murthy, A. C. Nilsson, R. A. Salvatore, M. F. Van Leeuwen, J. Webjorn, M. Ziari, S. G. Grubb, D. Perkins, M. Reffle, and D. G. Mehuys, IEEE J. Sel. Top. Quantum Electron. **13,** 22 (2007).
4. S. Corzine, P. Evans, M. Fisher, J. Gheorma, M. Kato, V. Dominic, P. Samra, A. Nilsson, J. Rahn, I. Lyubomirsky, A. Dentai, P. Studenkov, M. Missey, D. Lambert, A. Spannagel, R. Muthiah, R. Salvatore, S. Murthy, E. Strzelecka, J. L. Pleumeekers, A. Chen, R. Schneider, R. Nagarajan, M. Ziari, J. Stewart, C. H. Joyner, F. Kish, and D. F. Welch, IEEE Photon. Technol. Lett. **22,** 1015 (2010).
5. T. Fujisawa, S. Kanazawa, K. Takahata, W. Kobayashi, T. Tadokoro, H. Ishii, and F. Kano, Opt. Express **20,** 614 (2012).
6. H. Ishii, K. Kasaya, and H. Oohashi, IEEE J. Sel. Top. Quantum Electron. **15,** 514 (2009).
7. S. Sakamoto, T. Okamoto, T. Yamazaki, S. Tamura, and S. Arai, IEEE J. Sel. Top. Quantum Electron. **11,** 1174 (2005).
8. L. P. Hou, M. Haji, J. Akbar, J. H. Marsh, and A. C. Bryce, Opt. Lett. **36,** 4188 (2011).
9. G. P. Li, T. Makino, A. Sarangan, and W. Huang, IEEE Photon. Technol. Lett. **8,** 22 (1996).
10. Y. Shi, X. Chen, Y. Zhou, S. Li, L. Lu, R. Liu, and Y. Feng, Opt. Lett. **37,** 3315 (2012).
11. H. L. Zhu, X. D. Xu, H. Wang, D. H. Kong, S. Liang, L. J. Zhao, and W. Wang, IEEE Photon. Technol. Lett. **22,** 353 (2010).
12. M. Zanola, M. J. Strain, G. Giuliani, and M. Sorel, IEEE Photon. Technol. Lett. **24,** 1063 (2012).
13. N. Nunoya, H. Ishii, Y. Kawaguchi, R. Iga, T. Sato, N. Fujiwara, and H. Oohashi, IEEE J. Sel. Top. Quantum Electron. **17,** 1505 (2011).
14. L. J. P. Ketelsen, J. A. Grenko, S. K. Sputz, M. W. Focht, J. M. Vandenberg, J. E. Johnson, C. L. Reynolds, J. M. Geary, J. Levkoff, K. G. Glogovsky, D. V. Stampone, S. N. G. Chu, T. Siegrist, T. L. Pernell, F. S. Walters, J. Sheridan-Eng, J. L. Lentz, M. A. Alam, R. People, M. S. Hybertsen, E. D. Isaacs, K. Evans-Lutterodt, R. E. Leibenguth, G. J. Przybyiek, L. Zhang, K. Feder, S. Shunk, D. M. Tennant, L. J. Peticolas, D. M. Romero, J. M. Freund, B. S. Falk, N. N. Tzafaras, L. E. Smith, L. C. Luther, M. Geva, W. A. Gault, and J. L. Zilko, IEEE J. Quantum Electron. **36,** 641 (2000).
15. Y. B. Cheng, J. Q. Pan, Y. Wang, F. Zhou, B. J. Wang, L. J. Zhao, H. L. Zhu, and W. Wang, IEEE Photon. Technol. Lett. **21,** 356 (2009).
16. Q. Zhao, J. Q. Pan, J. Zhang, B. X. Li, F. Zhou, B. J. Wang, L. F. Wang, J. Bian, L. J. Zhao, and W. Wang, Opt. Commun. **260,** 666 (2006).
17. S. W. Ryu, J. S. Sim, Y. H. Kwan, S. B. Kim, and Y. S. Baek, Semicond. Sci. Technol. **23**, 055012 (2008).
18. T. Kihara, Y. Nitta, H. Suda, K. Miki, and K. Shimomura, J. Cryst. Growth **221,** 196 (2000).
19. K. S. Chiang, K. M. Lo, and K. S. Kwok, J. Lightwave Technol. **14,** 223 (1996).
20. A. Polemi, A. Alu, and N. Engheta, IEEE Antenn. Wireless Propag. Lett. **10,** 199 (2011).
21. Nishikata, H. Shimizu, K. Hiraiwa, S. Yoshida, N. Yamanaka, M. Irikawa, and A. Kasukawa, J. Cryst. Growth **175-176,** 990 (1997).